Novel extended Kalman filter + H optimal output feedback control configuration for small satellites with high pointing stability requirements

Received: 30 January 2023 | Revised: 3 October 2023 | Accepted: 15 November 2023

DOI: 10.1002/rnc.7119

RESEARCH ARTICLE

WILEY

Novel extended Kalman filter + H_∞ optimal output feedback control configuration for small satellites with high pointing stability requirements

Manuel Pecorilla | **Fabrizio Stesina**

Department of Mechanical and Aerospace Engineering, Politecnico di Torino, Torino, Italy

Correspondence
Fabrizio Stesina, Department of Mechanical and Aerospace Engineering, Politecnico di Torino, Corso Duca Degli Abruzzi, 24, Torino, Italy.
Email: fabrizio.stesina@polito.it

Summary

One of the most challenging subsystems for the CubeSats is the attitude determination and control system (ADCS) because it involves hardware and software integration, advanced strategies and algorithms to determine and control the attitude that impacts on space maneuvering and well working of a large set of payload (e.g., the optical payload). Although ADCS is largely studied, it still requires further investigations and analysis in order to achieve high-performance and a reduced efforts. This paper presents an effective and reliable solution for the ADCS of CubeSats involved in Earth observation missions. The solution is based on an innovative framework that leverages the strengths of two distinct methodologies—H-infinity optimal output feedback control and the extended Kalman filter (EKF)-to significantly enhance the pointing stability of satellite systems. While H-infinity optimal output feedback control is traditionally associated with partial state knowledge, we intentionally extend its application to scenarios with complete state information. The study includes a comparative performance analysis involving three algorithm configurations: the classic combination of EKF and model predictive control (MPC), the utilization of H-infinity optimal output feedback control without EKF, and our proposed integrated approach. Performance evaluations are based on extrinsic indicators, demonstrating the advantages of our method in terms of pointing stability and overall control system performance. This research underscore the significance of combining innovative thinking with well-established methodologies, unlocking new possibilities for stability enhancement in a range of engineering applications.

KEYWORDS

CubeSats, extended Kalman filter, H_∞ optimal output feedback control, robust control

Abbreviations: ADCS, attitude determination and control system; AKE, absolute knowledge error; APE, absolute performance error; ECSS, European cooperation for space standardization; EKF, extended Kalman filter; LMI, linear matrix inequalities; LTI, linear time invariant; MPC, model predictive control; PSE, performance stability error; SVD, singular value decomposition.

1 | INTRODUCTION

The last years observed a dramatic increment of the CubeSats in orbit due to the possibility to perform relevant and of interest space missions in a cheaper and quicker way. This increment is also due to the improvement of the operational capabilities[1] of this kind of satellites supported by the availability of new miniaturized technologies. Several missions, such as Earth,[2–4] and planetary[5] observation and On Orbit Servicing,[6,7] require increasingly high accuracy and pointing stability to allow payloads to acquire valuable data and images.[8] In this context, the attitude determination and control system (ADCS) plays a fundamental role because enable the capability to achieve and maintain a desired target or a subject pointing. Since the design of the ADCS for small satellites often involves low-cost hardware that provides poor performance, it is necessary to employ advanced algorithmic solutions based on effective algorithms to meet the stringent requirements on the attitude knowledge and the attitude and velocity control performance.[9]

The active determination and control system of a CubeSat is a well-established technology available on the market.[10] According to the CubeSats ADCS survey statistics in Reference 11, almost every CubeSat employs magnetometers, sun sensors, and gyroscopes for attitude determination. A low percentage of CubeSats adopt passive control techniques, while most use reaction wheels-based active attitude control strategies for precise pointing. Nowadays, many advanced attitude determination and control algorithms have been proposed. A large proportion of spacecraft attitude control algorithms utilize full state knowledge, for example, attitude and angular velocities feedback. As stated in Reference 12, the problem of controlling a spacecraft without full state feedback is more complex. The approaches used to solve this problem can be divided into methods which estimate the unmeasured states using a filter algorithm, and methods which develop control laws directly from output feedback.

A configuration of the attitude determination and control algorithms that falls into the first category involves a Kalman Filter that provides the satellite's attitude estimation to a control algorithm. The choice of the control algorithm depends on the application and the desired performances. A possible solution is to combine the optimal estimator with an optimal controller, such as the model predictive controller (MPC). In this case the algorithms are optimized separately and then used together. This is a commonly used solution, which is why it will be referred to as 'classic' in the following. Some examples in which such a configuration is implemented are References 13–15. Other instances of optimal controllers encompass adaptive controllers, and within this realm, recent studies harness the potential of AI. Notably, research on hierarchical sliding-mode surfaces (HSMS)-based[16] and sliding-mode surfaces (SMS)-based[17] adaptive optimal control exemplifies this trend. These innovative studies, utilizing the potential of actor-critic (AC) neural networks, highlight the growing integration of artificial intelligence in optimizing control performance, even within scenarios featuring complex dynamics and uncertainties.

An alternative solution that does not involve state estimators is to develop a control law that exploits output feedback only. Such solutions have been the subject of research for some time now, the purpose of which is to, for example, make angular velocity measurement unnecessary in attitude control. For example in Reference 18, the authors propose a quaternion-based dynamic output feedback for the attitude tracking problem of a rigid body without velocity measurement in which they utilize an auxiliary dynamical system. Another example is that discussed in Reference 19, where the authors propose a computational scheme for solving the nonlinear output-feedback H_∞ control problem for spacecraft attitude control.

Our paper intentionally applies a control methodology that is typically designed for partial state knowledge scenarios to a case where complete state knowledge is available. In this context, our study presents a unique approach by combining the H-infinity optimal output feedback control with the extended Kalman filter (EKF). This innovative combination aims at achieving relevant results in terms of pointing stability. This approach holds the potential to significantly enhance control system performance by harnessing the benefits of both approaches within a unified framework. To demonstrate the superiority of this combination, a comprehensive performance study is conducted, comparing it with two alternative algorithm configurations. The first configuration involves the classical combination of the EKF and MPC. The second configuration entails the utilization of the H-infinity optimal output feedback control, also with complete state knowledge, but without the incorporation of the EKF. This comparative performance analysis is based on extrinsic performance indicators, aiming to establish the advantages of our proposed approach in terms of pointing stability and overall control system performance. This evaluation will provide a clear assessment of the innovative synergy achieved by integrating the EKF with the H-infinity optimal output feedback control technique, showcasing its potential to outperform both the classical EKF-MPC combination and the standalone H-infinity control configuration. The study is carried out through simulations that include all the perturbations related to a spacecraft in low earth orbit and the measurement noises in the sensors used for attitude determination and angular velocity measurement.

TABLE 1 Technical requirements specification for the ADCS.

Requirement	Description
Absolute performance error (APE)	The ADCS shall ensure during the operational mission phase an absolute pointing performance of 0.65°, at 95% (2σ) confidence level
Control error	The ADCS shall ensure during the operational mission phase a control error less than 0.31°, at 95% (2σ) confidence level
Absolute knowledge error (AKE)	The ADCS shall ensure during the operational mission phase an on-board absolute knowledge performance of 0.31°, at 95% (2σ) confidence level
Performance stability error (PSE)	The ADCS shall ensure during the operational mission phase a pointing accuracy stability of 7.41 arcmin/s (0.12°/s), at 95% (2σ) confidence level

Note: The statistical interpretation for all requirements is the temporal interpretation.

1.1 | Context and objectives

The attention is focused on the field of small satellites used in earth observation missions. Taking images for observation payloads requires specific stability requirements to prevent blurring pictures acquisition and pointing accuracy requirements to focus the target. These requirements are defined according to extrinsic performance indicators in agreement with the European Cooperation for Space Standardization (ECSS) standard.[9] The case study considered in this paper uses the requirements shown in Table 1 related to a 3U CubeSat employed in an Earth observation mission as a reference. Such requirements derive from a payload performance study, system, and mission aspects.

The paper's objective is to illustrate the potential of a novel algorithmic synergy, demonstrating enhanced performance, particularly in terms of pointing stability, compared to conventional configurations. Specifically, these algorithms are deployed in the nadir pointing control mode, essential for stabilizing the CubeSat and aligning the observation payload's axis with the local vertical. The proposed solution combines the filtering capabilities of the EKF with the disturbance rejection and optimal controller properties of the H_∞ optimal output feedback controller, intentionally leveraging complete state knowledge. This deliberate integration is designed to result in exceptional pointing stability. For a comprehensive evaluation, two alternative algorithm configurations are incorporated, facilitating a performance comparison that unequivocally highlights the advantages of this innovative approach. The three configurations under study are those depicted in Figure 1 and include:

1. Optimal estimator and optimal controller: This configuration involves the classic combination of an extended Kalman filter and a model predictive controller.
2. Deterministic method and optimal output feedback controller: In this case, only the H_∞ controller is used together with the singular value decomposition (SVD) method required for the quaternion calculation.
3. Optimal estimator and optimal output feedback controller: In this case, the H_∞ controller is used together with the extended Kalman filter

As described in section 2.2, the SVD Method is used in this work to provide the EKF with the quaternion attitude measurement update. In the case of the output feedback configuration, the SVD method provides the attitude measurement directly to the H_∞ controller.

2 | PROBLEM FORMULATION

The background to this study concerns the dynamics of an Earth Observation satellite in the nadir pointing control mode. The general framework in which the dynamics of an Earth-Pointing spacecraft take place is highlighted in Figure 2, which illustrates a spacecraft orbiting in a generic orbit around the Earth. Four different reference systems can be identified[12]

1. Earth-Centered Inertial Frame ($\mathcal{F}_{ECI}$)
2. Earth-Centered Earth-Fixed Frame ($\mathcal{F}_{ECEF}$)
3. Local Orbital Frame ($\mathcal{F}_O$)
4. Spacecraft Body Frame ($\mathcal{F}_B$)

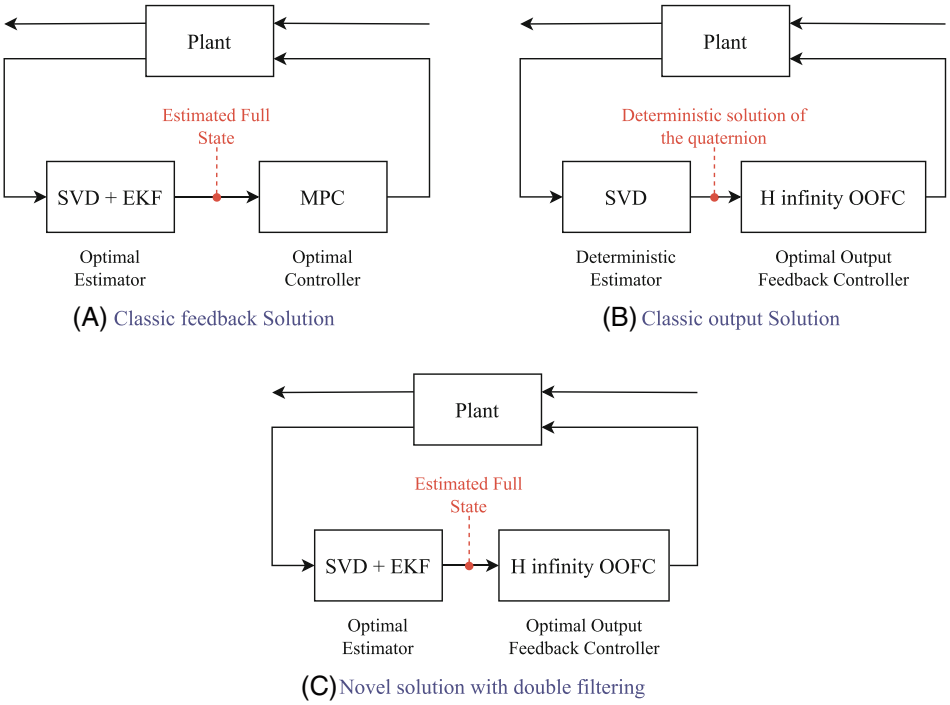

FIGURE 1 Attitude determination and control loop alternative configurations: (A) Classic feedback solution, (B) classic output solution, (C) novel solution with double filtering.

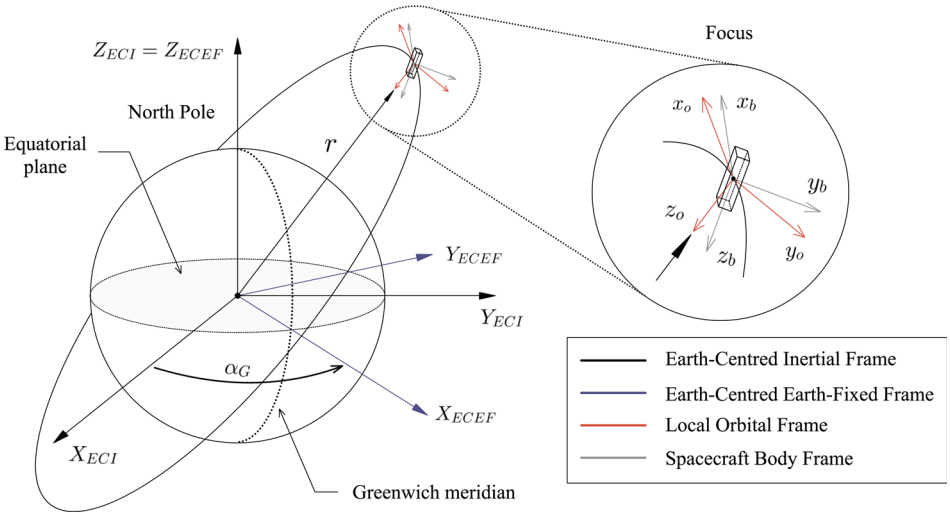

FIGURE 2 Main reference frames for the description of the dynamics of an earth pointing spacecraft.

The dynamics of a rigid spacecraft is intricately characterized by four key parameters: position, velocity, attitude, and angular velocity. These four factors collectively elucidate the spacecraft's complex motion through space. The initial pair, position and velocity, serve as fundamental descriptors of the translational motion exhibited by the spacecraft's center of mass. Conversely, the latter pair, attitude, and angular velocity, delve into the spacecraft's rotational dynamics around its center of mass.

2.1 | Spacecraft dynamic and kinematics

With reference to the coordinate frames delineated in Figure 2, we can articulate the equation governing the angular momentum of a rigid body with respect to the inertial reference frame $\mathcal{F}_{ECI}$. This equation offers insight into the dynamic

evolution of angular momentum, encompassing the effects induced by applied torques as well as the intrinsic variations over time.

$$\dot{\overline{h}}^B + \overline{\omega}_{IB}^B \times \overline{h}^B = \overline{T}^B \tag{1}$$

Equation (1) is the Euler's equation which characterize the dynamic of a rigid body around its center of mass with respect to an inertial frame. In the equation

1. $\overline{\omega}_{IB}^B$ is the angular velocity of the spacecraft relative to $\mathcal{F}_{ECI}$ expressed in the body frame $\mathcal{F}_B$;
2. $\overline{h}^B$ is the spacecraft's angular momentum vector measured in the body frame $\mathcal{F}_B$;
3. $\overline{T}^B$ includes all the external torques acting on the spacecraft with respect to its center of mass expressed in the body frame $\mathcal{F}_B$.

In the scenario where reaction wheels are integrated onboard a satellite, the total angular momentum of the satellite is composed of two distinct components. The first component arises from the satellite's inherent rotation, encapsulating the angular momentum generated by its own motion. The second component emanates from the rotation of the reaction wheels themselves. The collective sum of these two contributions yields the comprehensive total angular momentum of the satellite. Therefore, the angular momentum of the spacecraft expressed in $\mathcal{F}_B$ can be written as

$$\overline{h}^B = \mathbf{I}\overline{\omega}_{IB}^B + \mathbf{I}_{RW}\overline{\omega}_{RW} \tag{2}$$

where I is the inertia matrix of the spacecraft, which is assumed to be diagonal, I_{RW} is the inertia matrix of the wheels with respect to body frame, and $\overline{\omega}_{RW}$ is the angular velocity of the wheels.

By substituting (2) in Equation (1), the angular acceleration can be calculated as

$$\dot{\overline{\omega}}_{IB}^B = \mathbf{I}^{-1}\left(\overline{T}^B - \overline{\omega}_{IB}^B \times \left(\mathbf{I}\overline{\omega}_{IB}^B + \mathbf{I}_{RW}\overline{\omega}_{RW}\right)\right) \tag{3}$$

Integrating Equation (3) over time allows to obtain the angular velocity of the spacecraft. To evaluate the angular velocity relative to the local orbital frame expressed in $\mathcal{F}_B$ $\left(\overline{\omega}_{OB}^B\right)$ it is necessary to consider that

$$\overline{\omega}_{IB}^B = \overline{\omega}_{OB}^B + \mathbf{A}_O^B\overline{\omega}_{IO}^O \tag{4}$$

where $\overline{\omega}_{IO}^O = [0 \ -\omega_0 \ 0]$ is the angular velocity of the local orbital frame $\mathcal{F}_O$ relative to the inertial frame $\mathcal{F}_{ECI}$ expressed in $\mathcal{F}_O$. The scalar ω_0 is the angular velocity of the spacecraft about the Earth's center and can be calculated as

$$\omega_0 = \sqrt{\frac{\mu_E}{r^3}} \tag{5}$$

Once the angular velocity $\overline{\omega}_{OB}^B$ is known from Equation (4), the attitude of the spacecraft can be calculated. Using quaternions as attitude representation the attitude is given by integrating the following formulas

$$\dot{q}_0 = -\frac{1}{2}\,\overline{\omega}_{OB}^B\,\vec{q} \tag{6}$$

$$\dot{\vec{q}} = \frac{1}{2}\,q_0\,\overline{\omega}_{OB}^B + \frac{1}{2}\,\vec{q} \times \overline{\omega}_{OB}^B \tag{7}$$

$\vec{q}$ and q_0 are respectively the vector and scalar part of the quaternion.

2.2 | Attitude determination

In this section, it's important to clarify that the description of the attitude determination process and the subsequent utilization of measurements within the SVD and Kalman Filter algorithms serves a purely descriptive purpose. Its intention is to provide readers with essential background information to facilitate the understanding.

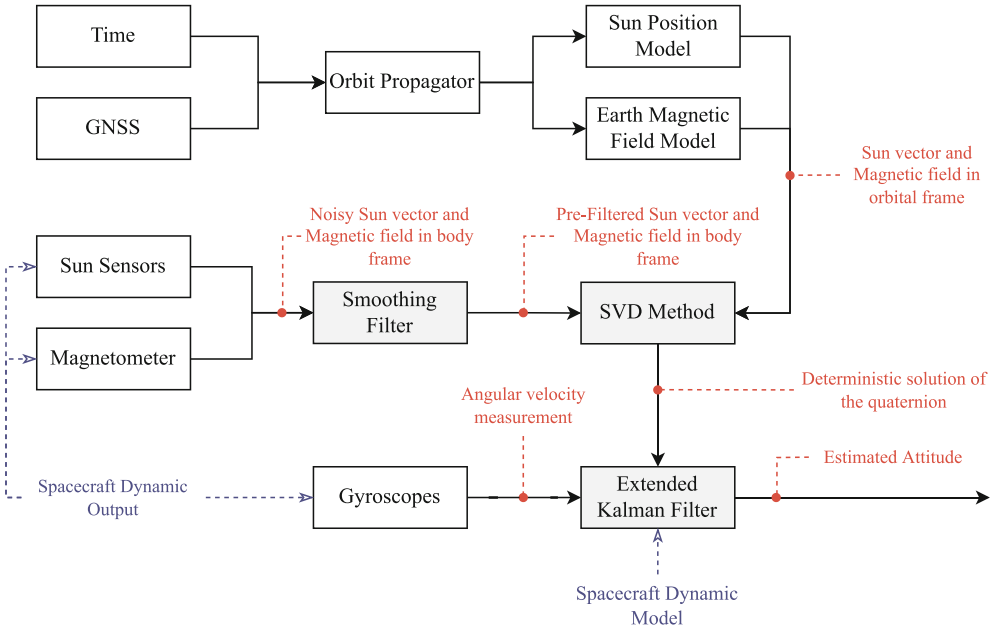

FIGURE 3 Schematic representation of the attitude determination algorithms operating logic.

The determination process is carried out by combining deterministic and recursive methods. The logical framework involves a procedure that sequentially employs a smoothing filter, the singular value decomposition method for deterministic determination, and an extended Kalman filter for recursive estimation. The workflow (Figure 3) begins with acquiring measurements, referred to the body frame $\mathcal{F}_B$, provided by the sun sensors and magnetometer at a frequency of 10 Hz. These measurements are noisy, so they are appropriately filtered using a smoothing filter before being used for attitude determination. At the same frequency, the processing unit calculates the corresponding vectors related to the local orbital frame $\mathcal{F}_O$ using suitable models for the Earth magnetic field[20] and Sun position.[21] Thus, two pairs of measurements are available for deterministic attitude estimation using the singular value decomposition method. This deterministic solution is then applied as innovation to update the estimate made by the EKF, which also provides the satellite's angular velocity using measurements from the gyroscopes and the satellite dynamic model.

The extended Kalman filter state vector elements includes the vector part of the quaternion, the three components of the angular velocity $\overline{\omega}^B_{IB}$ and the bias on the angular velocity measurements.

$$\hat{x} = \begin{bmatrix} q_1 & q_2 & q_3 & \omega^B_{IB_x} & \omega^B_{IB_y} & \omega^B_{IB_z} & \beta_x & \beta_y & \beta_z \end{bmatrix}^T \tag{8}$$

2.3 | Attitude control

Two control laws have been considered for the analysis:

1. Model predictive control law
2. H_∞ optimal output feedback control law

Both controllers considered use the state space model of the system in their synthesis. The relationships describing the kinematics and attitude dynamics are non-linear, so they cannot be written directly in the state space form. The linearization of the system mathematical model is performed around the equilibrium point, which in the considered case will be the nadir pointing attitude. In other words, unit quaternion approximation can be assumed.

$$\overline{q} = \begin{bmatrix} q_0 \\ \vec{q} \end{bmatrix} = \begin{bmatrix} q_0 \\ q_1 \\ q_2 \\ q_3 \end{bmatrix} \approx \begin{bmatrix} 1 \\ 0 \\ 0 \\ 0 \end{bmatrix} \tag{9}$$

The state space model is given by

$$\dot{\bar{x}} = \mathbf{A}\bar{x} + \mathbf{B}\bar{u} \tag{10}$$

where in this case the state vector $\bar{x}$ is composed by the vector part of the quaternion and the three components of the angular velocity $\bar{\omega}_{OB}^{B}$

$$\hat{x} = \begin{bmatrix} q_1 & q_2 & q_3 & \omega_x & \omega_y & \omega_z \end{bmatrix}^T \tag{11}$$

while $\bar{u}$ is the three components command torque vector, and the matrices **A** and **B** are defined as shown in Equation (12).

$$\mathbf{A} = \begin{bmatrix} 0 & 0 & 0 & 1/2 & 0 & 0 \\ 0 & 0 & 0 & 0 & 1/2 & 0 \\ 0 & 0 & 0 & 0 & 0 & 1/2 \\ -8\omega_0^2 \frac{I_y - I_z}{Ix} & 0 & 0 & 0 & 0 & \omega_0 \frac{I_z + I_x - I_y}{I_x} \\ 0 & -6\omega_0^2 \frac{I_x - I_z}{Iy} & 0 & 0 & 0 & 0 \\ 0 & 0 & -2\omega_0^2 \frac{I_y - I_x}{Iz} & -\omega_0 \frac{I_z + I_x - I_y}{I_z} & 0 & 0 \end{bmatrix} \quad \mathbf{B} = \begin{bmatrix} 0 & 0 & 0 \\ 0 & 0 & 0 \\ 0 & 0 & 0 \\ 1/I_x & 0 & 0 \\ 0 & 1/I_y & 0 \\ 0 & 0 & 1/I_z \end{bmatrix} \tag{12}$$

Modern control systems are typically implemented on a digital processor. The processor samples the sensors at discrete sampling instants and computes the corresponding control torques. The control torque is held constant according to the control frequency, thus following the logic of the so-called zero-order hold (ZOH) control implementation. For this reason, the controllers developed in this work are implemented in discrete time. The discrete version of the state space model is given by

$$\bar{x}(k+1) = \mathbf{A}_d \bar{x}(k) + \mathbf{B}_d \bar{u}(k) \tag{13}$$

where $\mathbf{A}_d$, and $\mathbf{B}_d$ can be calculated as

$$\mathbf{A}_d = e^{\mathbf{A}T_s} \quad \mathbf{B}_d = \int_0^{T_s} e^{\mathbf{A}\sigma} \mathbf{B} d\sigma \tag{14}$$

in the equations T_s is the control sampling time which is the inverse of the control frequency. Assuming that a measure of all state variables is available, the output equation can be written a

$$\bar{y}(k) = \mathbf{C}_d \, \bar{x}(k) \tag{15}$$

where $\mathbf{C}_d$ is the 6×6 square identity matrix.

2.3.1 | H_∞ optimal output feedback control

Systems for which controllers are designed inherently face uncertainties and disturbances arising from imperfect modeling, measurement errors, component imperfections, and other factors. Consequently, designing controllers capable of delivering optimal performance while mitigating the impact of these disturbance sources becomes imperative. This underscores the significance of the H_∞ controller, which is specifically devised to address this challenge. Its main goal can be succinctly articulated as follows.

Given a linear system, it is possible to introduce the control framework by separating input signals from output signals

1. Output signals
   (a) Regulated outputs z, outputs to be controlled
   (b) Sensed outputs y, outputs used by the controller
2. Input signals
   (a) Exogenous inputs w, disturbances, tracking signals, and so forth.
   (b) Actuator inputs u, output from the controller

The controller closes the loop from y to u as shown in Figure 4.

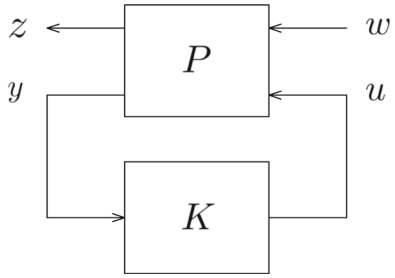

FIGURE 4 The optimal control framework.

This sets up the framework for H_∞ optimal control whose goal is to choose the controller K such that the map from exogenous inputs (disturbances) to regulated outputs is minimized. This is equivalent to minimizing the closed-loop system L_2 induced norm which is the H_∞ norm of the transfer function realization. As reported in Reference 22 the synthesis method for the H_∞ optimal output feedback controller is given by the optimization problem (16) with linear matrix inequalities.

$$\min_{\gamma,\ \mathbf{X}_1,\ \mathbf{Y}_1,\ \mathbf{A}_{dn},\ \mathbf{B}_{dn},\ \mathbf{C}_{dn},\ \mathbf{D}_{dn},\ \mathbf{G},\ \mathbf{H},\ \mathbf{J},\ \mathbf{S}} \quad \gamma$$

subject to

$$\begin{bmatrix} \mathbf{X}_1 & \mathbf{J}^T & \mathbf{H}\mathbf{A}_d + \mathbf{B}_{dn}\mathbf{C}_{d2} & \mathbf{A}_{dn} & \mathbf{H}\mathbf{B}_{d1} + \mathbf{B}_{dn}\mathbf{D}_{d21} & \mathbf{0} \\ * & \mathbf{Y}_1 & \mathbf{A}_d + \mathbf{B}_{d2}\mathbf{D}_{dn}\mathbf{C}_{d2} & \mathbf{A}_d\mathbf{G} + \mathbf{B}_{d2}\mathbf{C}_{dn} & \mathbf{B}_{d1} + \mathbf{B}_{d2}\mathbf{D}_{dn}\mathbf{D}_{d21} & \mathbf{0} \\ * & * & \mathbf{H} + \mathbf{H}^T - \mathbf{X}_1 & \boldsymbol{\mathcal{I}} + \mathbf{S} - \mathbf{J}^T & \mathbf{0} & \mathbf{C}_{d1}^T + \mathbf{C}_{d2}^T\mathbf{D}_{dn}^T\mathbf{D}_{d12}^T \\ * & * & * & \mathbf{Y}_1 & \mathbf{0} & \mathbf{Y}_1\mathbf{C}_{d1}^T + \mathbf{C}_{dn}^T\mathbf{D}_{d12}^T \\ * & * & * & * & \gamma\boldsymbol{\mathcal{I}} & \mathbf{D}_{d11}^T + \mathbf{D}_{d21}^T\mathbf{D}_{dn}^T\mathbf{D}_{d12}^T \\ * & * & * & * & * & \gamma\boldsymbol{\mathcal{I}} \end{bmatrix} > 0$$

$$\mathbf{X}_1 > 0, \mathbf{Y}_1 > 0 \tag{16}$$

The controller is recovered by

$$\begin{aligned} \mathbf{D}_K &= (\boldsymbol{\mathcal{I}} + \mathbf{D}_{dK}\mathbf{D}_{d22})^{-1}\mathbf{D}_{dK} \\ \mathbf{C}_K &= (\boldsymbol{\mathcal{I}} - \mathbf{D}_K\mathbf{D}_{d22})\mathbf{C}_{dK} \\ \mathbf{B}_K &= \mathbf{B}_{dK}(\boldsymbol{\mathcal{I}} - \mathbf{D}_{d22}\mathbf{D}_K) \\ \mathbf{A}_K &= \mathbf{A}_{dK} - \mathbf{B}_K(\boldsymbol{\mathcal{I}} - \mathbf{D}_{d22}\mathbf{D}_K)^{-1}\mathbf{D}_{d22}\mathbf{C}_K \end{aligned} \tag{17}$$

where

$$\left[\begin{array}{c|c} \mathbf{A}_{dK} & \mathbf{B}_{dK} \\ \hline \mathbf{C}_{dK} & \mathbf{D}_{dK} \end{array}\right] = \begin{bmatrix} \mathbf{Y}_2^{-T} & \mathbf{Y}_2^{-T}\mathbf{H}\mathbf{B}_{d2} \\ \mathbf{0} & \boldsymbol{\mathcal{I}} \end{bmatrix} \left(\begin{bmatrix} \mathbf{A}_{dn} & \mathbf{B}_{dn} \\ \mathbf{C}_{dn} & \mathbf{D}_{dn} \end{bmatrix} - \begin{bmatrix} \mathbf{H}\mathbf{A}_d\mathbf{G} & \mathbf{0} \\ \mathbf{0} & \mathbf{0} \end{bmatrix} \right) \begin{bmatrix} \mathbf{X}_2^{-1} & \mathbf{0} \\ -\mathbf{C}_{d2}\mathbf{G}\mathbf{X}_2^{-1} & \boldsymbol{\mathcal{I}} \end{bmatrix} \tag{18}$$

and the matrices $\mathbf{X}_2$ and $\mathbf{Y}_2$ satisfy $\mathbf{X}_2\mathbf{Y}_2^T = \boldsymbol{\mathcal{I}} - \mathbf{H}\mathbf{G}$. If $\mathbf{D}_{d22} = 0$, then $\mathbf{A}_K = \mathbf{A}_{dK}$, $\mathbf{B}_K = \mathbf{B}_{dK}$, $\mathbf{C}_K = \mathbf{C}_{dK}$, and $\mathbf{D}_K = \mathbf{D}_{dK}$. Given $\mathbf{G}$ and $\mathbf{H}$, the matrices $\mathbf{X}_2$ and $\mathbf{Y}_2$ can be found using a matrix decomposition, such as a LU decomposition or a Cholesky decomposition.

The LMI in (16) is derived from the LMI in theorem 8 of Reference 23, where the proofs are also provided. This is achieved by performing a congruence transformation involving a multiplication on the left and right by the symmetric matrix

$$\mathbf{W} = \text{diag}\left\{ \begin{bmatrix} \mathbf{0} & \sqrt{\gamma}\boldsymbol{\mathcal{I}} \\ \frac{1}{\sqrt{\gamma}}\boldsymbol{\mathcal{I}} & \mathbf{0} \end{bmatrix}, \begin{bmatrix} \mathbf{0} & \sqrt{\gamma}\boldsymbol{\mathcal{I}} \\ \frac{1}{\sqrt{\gamma}}\boldsymbol{\mathcal{I}} & \mathbf{0} \end{bmatrix}, \sqrt{\gamma}\boldsymbol{\mathcal{I}}, \frac{1}{\sqrt{\gamma}}\boldsymbol{\mathcal{I}} \right\} \tag{19}$$

followed by the change of variables $\gamma = \mu^2, \mathbf{X}_1 = \gamma\mathbf{H}, \mathbf{Y}_1 = \gamma^{-1}\mathbf{P}$.

The same LMI (16) can be rewritten by performing the variables change $\mathbf{S} = \mathbf{J} = \boldsymbol{\mathcal{I}}$, $\mathbf{H} = \mathbf{X}_1$, $\mathbf{G} = \mathbf{Y}_1$, resulting in the LMI (20).

$$\min_{\gamma,\ \mathbf{X}_1,\ \mathbf{Y}_1,\ \mathbf{A}_{dn},\ \mathbf{B}_{dn},\ \mathbf{C}_{dn},\ \mathbf{D}_{dn}} \quad \gamma$$

subject to

$$\begin{bmatrix} \mathbf{X}_1 & \boldsymbol{\mathcal{I}} & \mathbf{X}_1\mathbf{A}_d + \mathbf{B}_{dn}\mathbf{C}_{d2} & \mathbf{A}_{dn} & \mathbf{X}_1\mathbf{B}_{d1} + \mathbf{B}_{dn}\mathbf{D}_{d21} & \mathbf{0} \\ * & \mathbf{Y}_1 & \mathbf{A}_d + \mathbf{B}_{d2}\mathbf{D}_{dn}\mathbf{C}_{d2} & \mathbf{A}_d\mathbf{Y}_1 + \mathbf{B}_{d2}\mathbf{C}_{dn} & \mathbf{B}_{d1} + \mathbf{B}_{d2}\mathbf{D}_{dn}\mathbf{D}_{d21} & \mathbf{0} \\ * & * & \mathbf{X}_1 & \boldsymbol{\mathcal{I}} & \mathbf{0} & \mathbf{C}_{d1}^T + \mathbf{C}_{d2}^T\mathbf{D}_{dn}^T\mathbf{D}_{d12}^T \\ * & * & * & \mathbf{Y}_1 & \mathbf{0} & \mathbf{Y}_1\mathbf{C}_{d1}^T + \mathbf{C}_{dn}^T\mathbf{D}_{d12}^T \\ * & * & * & * & \gamma\boldsymbol{\mathcal{I}} & \mathbf{D}_{d11}^T + \mathbf{D}_{d21}^T\mathbf{D}_{dn}^T\mathbf{D}_{d12}^T \\ * & * & * & * & * & \gamma\boldsymbol{\mathcal{I}} \end{bmatrix} > 0$$

$$\mathbf{X}_1 > 0, \mathbf{Y}_1 > 0$$

$$\begin{bmatrix} \mathbf{X}_1 & \boldsymbol{\mathcal{I}} \\ \boldsymbol{\mathcal{I}} & \mathbf{Y}_1 \end{bmatrix} > 0 \tag{20}$$

The controller is recovered by Equation (17), where in this case

$$\left[\begin{array}{c|c} \mathbf{A}_{dK} & \mathbf{B}_{dK} \\ \hline \mathbf{C}_{dK} & \mathbf{D}_{dK} \end{array}\right] = \begin{bmatrix} \mathbf{X}_2 & \mathbf{X}_1\mathbf{B}_{d2} \\ \mathbf{0} & \boldsymbol{\mathcal{I}} \end{bmatrix}^{-1} \left(\begin{bmatrix} \mathbf{A}_{dn} & \mathbf{B}_{dn} \\ \mathbf{C}_{dn} & \mathbf{D}_{dn} \end{bmatrix} - \begin{bmatrix} \mathbf{X}_1\mathbf{A}_d\mathbf{Y}_1 & \mathbf{0} \\ \mathbf{0} & \mathbf{0} \end{bmatrix} \right) \begin{bmatrix} \mathbf{Y}_2^T & \mathbf{0} \\ \mathbf{C}_{d2}\mathbf{Y}_1 & \boldsymbol{\mathcal{I}} \end{bmatrix}^{-1} \tag{21}$$

and where $\mathbf{X}_2$ and $\mathbf{Y}_2$ are any matrices which satisfy $\mathbf{X}_2\mathbf{Y}_2^T = \boldsymbol{\mathcal{I}} - \mathbf{X}_1\mathbf{Y}_1$. The final LMI in (20) is added to ensure that $\boldsymbol{\mathcal{I}} - \mathbf{X}_1\mathbf{Y}_1 \geq \mathbf{0}$ in a similar fashion to the approach used in Reference 24.

The matrices $\mathbf{A}_d$, $\mathbf{B}_{d1}$, $\mathbf{B}_{d2}$, $\mathbf{C}_{d1}$, $\mathbf{D}_{d11}$, $\mathbf{D}_{d12}$, $\mathbf{C}_{d2}$, $\mathbf{D}_{d21}$, $\mathbf{D}_{d22}$ featured in the optimization problem correspond to the matrix representation of the system, characterizing the discrete-time generalized linear time-invariant (LTI) plant P shown in Figure 4. The explicit relationship is outlined below:

$$\begin{aligned} \bar{x}(k+1) &= \mathbf{A}_d\ \bar{x}(k) + \mathbf{B}_{d1}\ \bar{w}(k) + \mathbf{B}_{d2}\ \bar{u}(k) \\ \bar{z}(k) &= \mathbf{C}_{d1}\ \bar{x}(k) + \mathbf{D}_{d11}\ \bar{w}(k) + \mathbf{D}_{d12}\ \bar{u}(k) \\ \bar{y}(k) &= \mathbf{C}_{d2}\ \bar{x}(k) + \mathbf{D}_{d21}\ \bar{w}(k) + \mathbf{D}_{d22}\ \bar{u}(k) \end{aligned} \tag{22}$$

where

1. $\bar{x}(k) = \begin{bmatrix} q_1 & q_2 & q_3 & \omega_x & \omega_y & \omega_z \end{bmatrix} \in \mathbb{R}^n$ is the system state vector at time step k;
2. $\bar{z}(k) = \begin{bmatrix} \bar{z}_1 & \bar{z}_2 \end{bmatrix} \in \mathbb{R}^{q+m}$ is the performance signal at time step k;
3. $\bar{y}(k) \in \mathbb{R}^q$ is the sensed output at time step k;
4. $\bar{w}(k) \in \mathbb{R}^q$ is the exogenous input at time step k;
5. $\bar{u}(k) \in \mathbb{R}^q$ is the control input at time step k;

where q is the number of output variables, n is the number of the state variables, and m is the number of control input variables.

To derive an expression for the nine matrices as a function of the matrices ($\mathbf{A}_d$, $\mathbf{B}_d$, $\mathbf{C}_d$, $\mathbf{D}_d$), constituting the state space representation of the nominal plant P_0, it is necessary to formulate the control problem in the two-input/two-output framework. In order to have a controller that can also track a desired attitude, other than the nadir pointing attitude, the tracking control framework, shown in Figure 5, has been implemented. The depicted framework shows the aggregate system P which can be seen in Figure 4. The exogenous inputs includes the reference signal $\bar{r}$, process noise $\bar{n}_{proc}$, and sensor noise indicated as $\bar{n}_{dist}$. To allow adjust performances it is possible to introduce weights within the framework. Although these could be tuned as a function of frequency, it was decided to use constant weights and thus diagonal matrices.

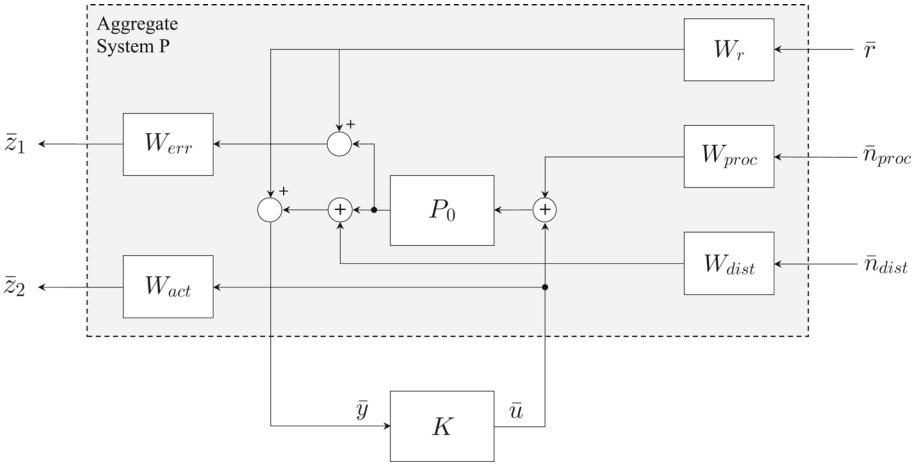

FIGURE 5 Tracking control framework.

The weights considered are the following:

1. $\mathbf{W}_{proc}$ is a $m \times m$ diagonal matrix for process noises;
2. $\mathbf{W}_{dist}$ is a $q \times q$ diagonal matrix for sensor noises;
3. $\mathbf{W}_{err}$ is a $q \times q$ diagonal matrix for errors between the desired and the actual signal;
4. $\mathbf{W}_{act}$ is a $m \times m$ diagonal matrix for control authority;
5. $\mathbf{W}_r$ is a $q \times q$ diagonal matrix for the reference signal;

For clarity, from now on the quantities relating to the plant P_0 are indicated by the subscript p, while only the initial of the weights' subscript is kept. By referring to Figure 5, the following equations can be written

$$\begin{aligned}
\bar{z}_1 &= \mathbf{W}_e \left[\mathbf{W}_r \bar{r} - P_0(\mathbf{W}_p\, \bar{n}_{proc} + \bar{u})\right] \\
\bar{z}_2 &= \mathbf{W}_a\, \bar{u} \\
\bar{y} &= \mathbf{W}_r \bar{r} - \left[P_0(\mathbf{W}_p\, \bar{n}_{proc} + \bar{u}) + \mathbf{W}_d\, \bar{n}_{dist}\right]
\end{aligned} \tag{23}$$

The input and the output of the system are

$$\begin{aligned}
\bar{u}_p &= \mathbf{W}_p\, \bar{n}_{proc} + \bar{u} \\
\bar{y}_p &= P_0(\mathbf{W}_p\, \bar{n}_{proc} + \bar{u})
\end{aligned} \tag{24}$$

While the state-space equations for the states and the output are

$$\begin{aligned}
\bar{x}_p(k+1) &= \mathbf{A}_d \bar{x}_p(k) + \mathbf{B}_d \bar{u}_p(k) \\
\bar{y}_p(k) &= \mathbf{C}_d \bar{x}_p(k) + \mathbf{D}_d \bar{u}_p(k)
\end{aligned} \tag{25}$$

Substituting $\bar{y}_p$ defined in Equation (25) into relation (23) gives

$$\begin{aligned}
\bar{z}_1 &= -\mathbf{W}_e \mathbf{C}_d \bar{x}_p + \mathbf{W}_e \mathbf{W}_r \bar{r} - \mathbf{W}_e \mathbf{D}_d \mathbf{W}_p\, \bar{n}_{proc} + \mathbf{W}_e \mathbf{D}_d \bar{u} \\
\bar{z}_2 &= \mathbf{W}_a\, \bar{u} \\
\bar{y} &= -\mathbf{C}_d \bar{x}_p + \mathbf{W}_r \bar{r} - \mathbf{D}_d \mathbf{W}_p\, \bar{n}_{proc} - \mathbf{W}_d\, \bar{n}_{dist} - \mathbf{D}_d \bar{u}
\end{aligned} \tag{26}$$

Therefore, the state-space realization defined in (22) can be written as

$$\begin{aligned}
\bar{x}(k+1) &= \mathbf{A}_d\, \bar{x}(k) + \begin{bmatrix} \mathbf{0} & \mathbf{B}_d \mathbf{W}_p & \mathbf{0} \end{bmatrix} \bar{w}(k) + \mathbf{B}_d\, \bar{u}(k) \\
\bar{z}(k) &= \begin{matrix} -\mathbf{W}_e \mathbf{C}_d \\ \mathbf{0} \end{matrix} \bar{x}(k) + \begin{bmatrix} \mathbf{W}_e \mathbf{W}_r \boldsymbol{\mathcal{I}} & -\mathbf{W}_e \mathbf{D}_d \mathbf{W}_p & \mathbf{0} \\ \mathbf{0} & \mathbf{0} & \mathbf{0} \end{bmatrix} \bar{w}(k) + \begin{bmatrix} -\mathbf{W}_e \mathbf{D}_d \\ \mathbf{W}_a \boldsymbol{\mathcal{I}} \end{bmatrix} \bar{u}(k) \\
\bar{y}(k) &= -\mathbf{C}_d\, \bar{x}(k) + \begin{bmatrix} \mathbf{W}_r \boldsymbol{\mathcal{I}} & -\mathbf{D}_d\, \mathbf{W}_p & -\mathbf{W}_d \boldsymbol{\mathcal{I}} \end{bmatrix} \bar{w}(k) - \mathbf{D}_d\, \bar{u}(k)
\end{aligned} \tag{27}$$

where

1. $\bar{x} = \bar{x}_p$
2. $\bar{w}^T(k) = \left[\bar{r}^T(k) \quad \bar{n}^T_{proc}(k) \quad \bar{n}^T_{dist}(k)\right]$
3. $\bar{u}(k) = \bar{u}_c(k)$
4. $\bar{y}(k) = \bar{r}(k) - \bar{y}_p(k) - \bar{n}_{dist}(k)$

Equation (27) give expressions for the nine matrix representation to be used in the optimization problem. The optimization problem has been solved in MATLAB using the YALMIP* toolbox.[25] The controller resulting from the optimization is a full order controller with internal dynamics which ensures the asymptotic stability of the closed-loop system while minimizing the gain between $\bar{w}$ and $\bar{z}$.

3 | MODELS AND SIMULATION

3.1 | MATLAB/Simulink model

The simulations are carried out using a six-degree-of-freedom orbital simulator (Figure 6). The diagram begins and ends with thicker boxes marking the beginning and end of the iterative loop. The simulator consists of the disturbance's models, the dynamics and kinematics model of the plant, the determination and control algorithms, and the actuator and sensor models. The new state vector and time are available at the beginning of each timestep. Time is required for the Julian date calculation, which is necessary to estimate the Moon and Sun's position and serves as input for computing the magnetic field.

The simulation state vector is defined as follows

$$\bar{x}_{\text{sim}} = \left[\bar{r} \quad \bar{v} \quad \bar{q} \quad \bar{\omega}^B_{IB} \quad \bar{\omega}_{RW}\right]^T \tag{28}$$

where

1. $\bar{r}$ is the spacecraft position
2. $\bar{v}$ is the spacecraft velocity
3. $\bar{q}$ is the quaternion
4. $\bar{\omega}^B_{IB}$ is the inertial referenced spacecraft angular velocity measured in the body frame
5. $\bar{\omega}_{RW}$ is the angular velocity of the reaction wheels

The spacecraft position and velocity, with the Sun and Moon positions, are used to calculate the orbital perturbations. Some of the perturbative forces are used then for the calculation of disturbance torques acting on the spacecraft.

The sensor model receives as input the angular velocity of the spacecraft, the measurement of the sun vector, and the Earth's magnetic field. These measurements are corrupted with noise resulting from the characteristics of the selected hardware. The noisy measurements of the sun vector and magnetic field are filtered by the smoothing filter and given as input, together with the respective models measured in the orbital frame, to the SVD method. The attitude obtained by the deterministic algorithm, represented by the quaternion, serves as an innovation for the extended Kalman filter with the angular velocity measurement acquired by gyroscopes. The output of the EKF is the recursive estimate of the attitude and angular velocity. Given these two quantities, it is possible to calculate the orbit-referenced angular rate of the spacecraft.

According to the current control mode, the ADCS state machine provides guidance for the controller. The estimated and desired quaternion and angular velocity are the input for the controller, which is responsible for reducing the error to zero. The controller produces a control torque applied by driving the reaction wheels. The latter and disturbance torques contribute to the dynamics of the spacecraft. The angular momentum of the reaction wheels must also be considered in the dynamics.

The kinematic and dynamic models of the spacecraft allow computing the variances of the quantities constituting the state vector. The angular acceleration of the reaction wheels is also part of the state vector to account for the dynamics of the wheels. The derivative of the state vector is integrated using the fourth-order Runge-Kutta numerical integration method. It marks the end of the current time step simulation loop and the beginning of the new one. The sensors were modeled for the simulations by considering an appropriate noise in the measurement resulting from considerations

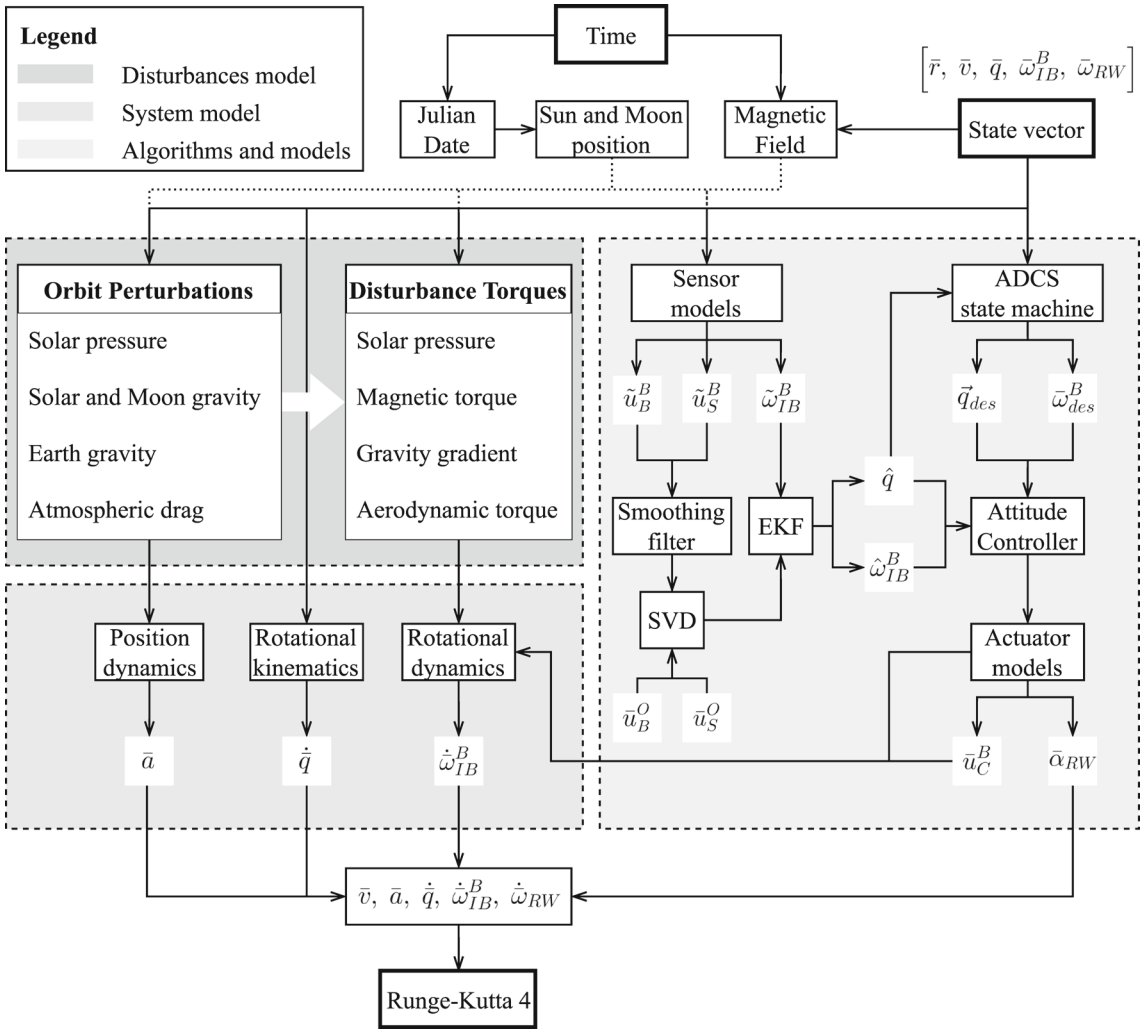

FIGURE 6 Representative diagram of the orbital simulator.

TABLE 2 Characteristic noises utilized to model the non-perfect working of the sensors in the simulations.

Sensor	Noise	Value	σ	Units	Notes
Sun Sensors	Bias	[−0.001, 0.001]	—	—	Uniformly distributed
	Output noise	[−0.05, 0.05]	—	—	Uniformly distributed
Gyroscopes	Bias†	[−0.045, 0.045]	0.0135	$deg/s^{3/2}$	Normal distributed, zero mean
	Output noise	[−0.81 0.81]	0.27	deg/s	Normal distributed, zero mean
Magnetometers	Output noise	[−5, 5]	—	μT	Uniformly distributed

Note: All noises listed are white noises.
† RRW, Rate random walk utilized in the gyroscope model and which causes drift rate.

regarding the selected hardware and based on previous experience. The noise characteristics used for the sensors is shown in Table 2. Regarding the actuators, four reaction wheels were modeled in a pyramidal configuration.

3.2 | Simulation results

This section presents the results from the performance comparison of the configurations presented in Figure 1. The comparison was performed based on the extrinsic indicators previously mentioned and considering other aspects

TABLE 3 Nadir pointing simulation setup.

Orbit characteristics	Circular orbit, Altitude = 470 km, Inclination = deg 51.6
Initial attitude	$[\Phi, \quad \Theta, \quad \Psi] = [-15, \quad 25, \quad 10]$ $[deg]$
Initial angular rates	$[\omega_x, \quad \omega_y, \quad \omega_z] = [0, \quad 0.0011, \quad 0]$ $[rad/s]$
Rates	Control rate = 0.5 s, Sampling rate = 0.1 s
Controller gains	
H_∞	Same weights as in Table 4
MPC	$\mathbf{Q} = 1000 \cdot \boldsymbol{\mathcal{I}}_n$, $\mathbf{R}_w = 1000 \cdot \boldsymbol{\mathcal{I}}_m$, $N_p = 10$, $N_c = 7$

TABLE 4 Weights used in the H_∞ controller simulation.

$\mathbf{W}_{act} = 1 \times 10^{-2}\ \mathrm{diag}\begin{bmatrix}1 & 1 & 1\end{bmatrix}$
$\mathbf{W}_{proc} = 2.5 \times 10^{-4}\ \mathrm{diag}\begin{bmatrix}1.2 & 1.2 & 0.25\end{bmatrix}$
$\mathbf{W}_{dist} = 5 \times 10^{-2}\ \mathrm{diag}\begin{bmatrix}1 & 1 & 1 & 1 & 1 & 1\end{bmatrix}$
$\mathbf{W}_{err} = 1 \times 10^{-5}\ \mathrm{diag}\begin{bmatrix}1 & 1 & 1 & 0.1 & 0.1 & 0.1\end{bmatrix}$
$\mathbf{W}_{r} = 2 \times 10^{-2}\ \mathrm{diag}\begin{bmatrix}1 & 1 & 1 & 0.1 & 0.1 & 0.1\end{bmatrix}$

characterizing the control efficiency as, for example, the cost of the attitude manoeuvre. Three simulations were carried out with the same initial conditions, shown in Tables 3 and 4, one for each configuration considered. Each simulation consists of using the previously discussed algorithms to control the spacecraft to reach the nadir pointing attitude from the specified initial conditions. These simulations were carried out over a time span of approximately 1000 s, but the plots are presented over shorter time intervals to highlight the trend of some variables.

The first results presented are those for quaternions and angular velocities shown in Figures 7 and 8. One difference that is immediately noticeable concerns how the quantities approach steady-state values. It is easy to see that the EKF+MPC configuration is much more direct in driving the state to the desired value. This suggests that the MPC controller exerts more costly control than the configurations with the H_∞ controller. A confirmation of this is provided by Figure 9 which shows angular velocities and accelerations of the reaction wheels. Figures 7, 8, and 9 show that the H_∞ controller configuration represents an effective trade-off between performance and control cost, as it allows for achieving good performance with small control torques. From these initial comparisons, it can be concluded that the EKF+MPC configuration is characterized by a more costly control when compared to the configurations with the H_∞ controller, but that allows better performance in terms of rise time.

In-depth analysis and comparison of the performance across these configurations are conducted through the consideration of extrinsic indicators such as APE, AKE, PSE, and the control error. These metrics provide a comprehensive assessment, allowing for a nuanced evaluation. For a detailed understanding of these indicators and their mathematical calculation, we refer to the comprehensive discussion in Reference 9. The ADCS requirements, as elucidated in Section 1.1 and detailed within Table 1, were originally specified in terms of angles. Consequently, it becomes advantageous to transition from quaternion-based representations to Euler angles. This shift offers a more immediate and visually intuitive interpretation of the results, simplifying the process of verifying compliance with the stipulated requirements.

Figures 10, 11, 12, and 13 show these indicators with a focus on the steady-state region. The diagrams also show the boundaries within which the requirement is fulfilled. To calculate the indicators in the case of the SVD+H_∞ configuration, the output of the SVD method is assumed to be the same as the estimate in the case of the EKF.

From Figure 10, it can be seen that the EKF+MPC and EKF+H_∞ configurations perform approximately similarly in terms of Absolute Knowledge Error. In contrast, the SVD+ H_∞ configuration does not meet the requirement stably. Consequently, it indicates that the application of the Extended Kalman Filter results in a better estimation than the

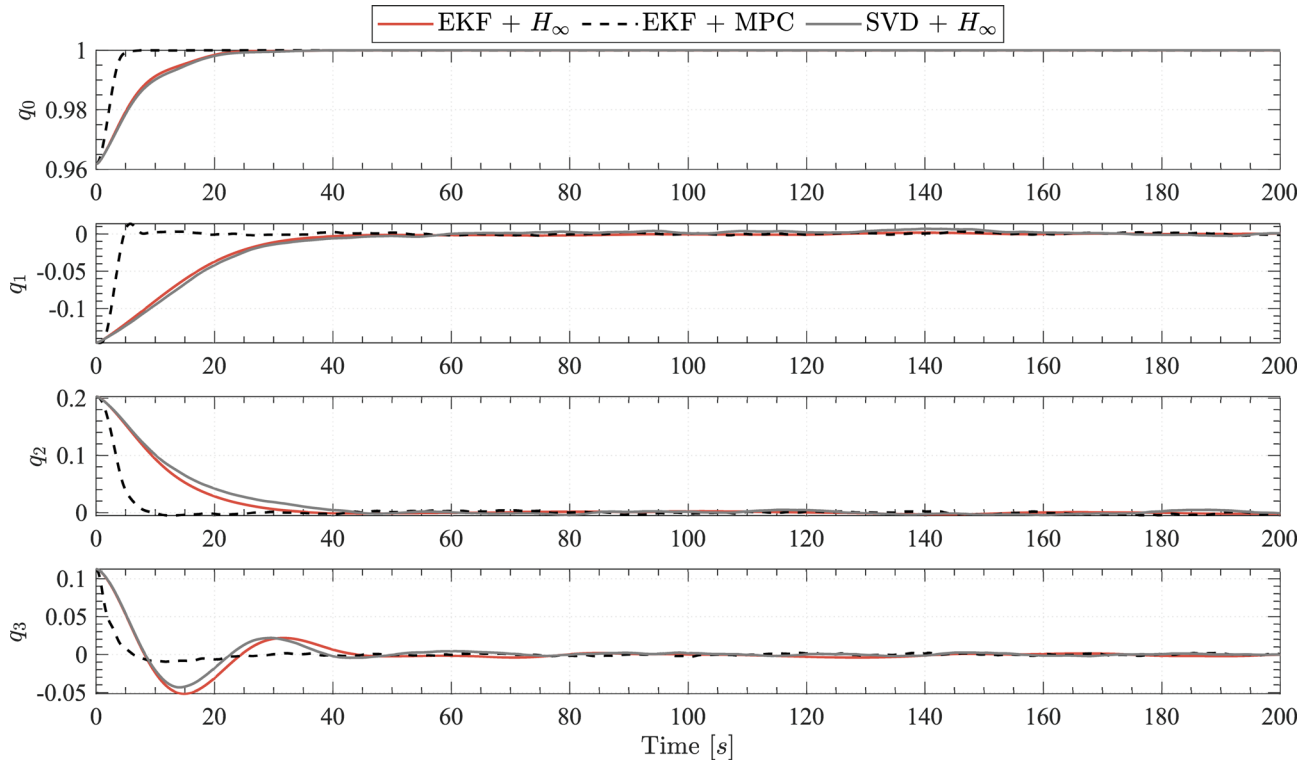

FIGURE 7 Comparison of the quaternions resulting from the nadir pointing simulation.

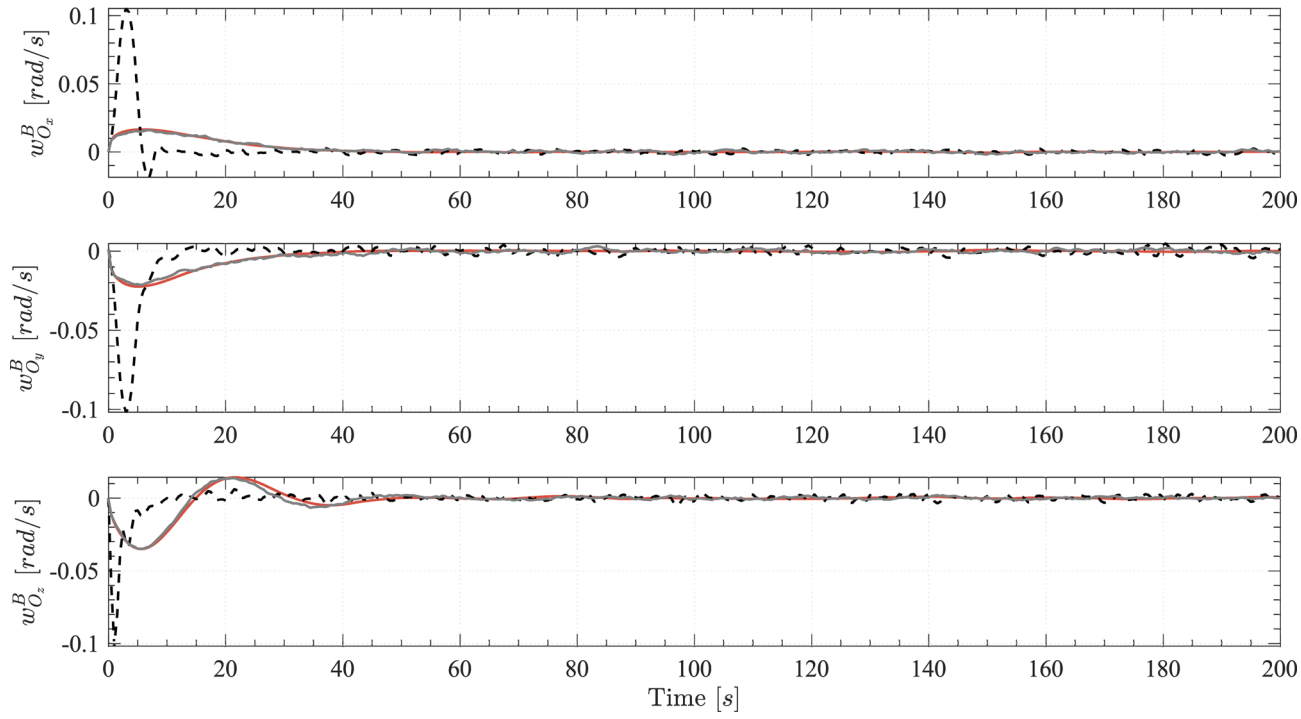

FIGURE 8 Comparison of the spacecraft angular velocities resulting from the nadir pointing simulation.

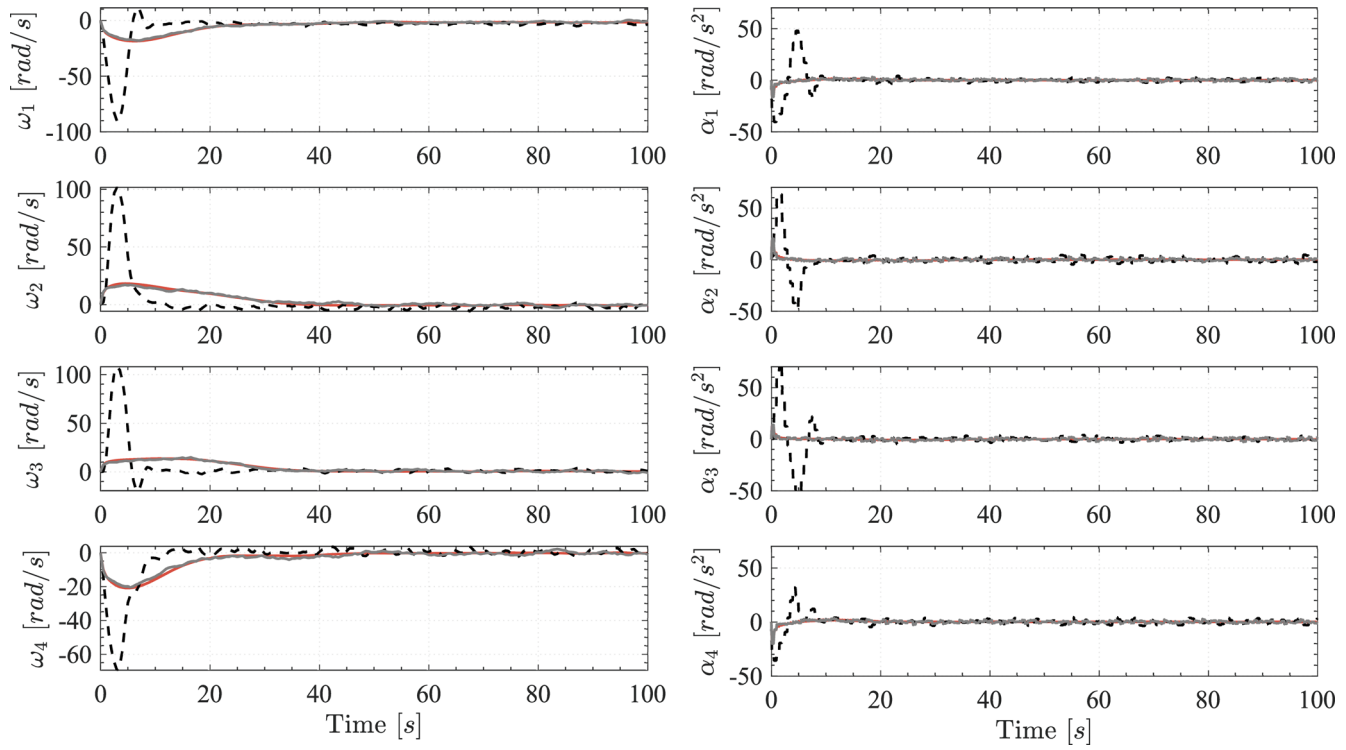

FIGURE 9 Comparison of the reaction wheels' accelerations and angular velocities resulting from the nadir pointing simulation.

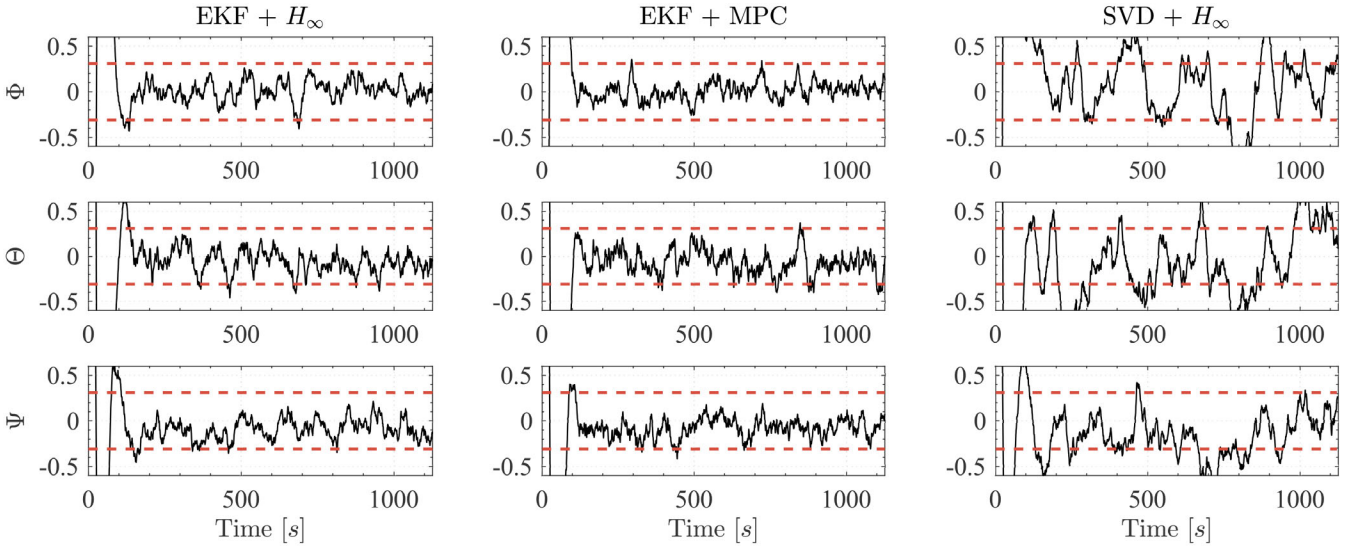

FIGURE 10 Absolute knowledge error (AKE) on Euler angles for the three configurations, resulting from the nadir pointing simulation. The boundaries indicate the region in which the requirement defined in Table 1 is met.

application of the SVD method alone. However, it should be emphasized that the latter comparison is only possible due to the noise attenuation properties of the H_∞ controller. The SVD method, in contrast to the EKF, cannot handle measurement noise, so a noisy input produces a noisy output. The same configuration but with the MPC controller instead of the H_∞ controller would not even be able to stabilize the spacecraft.

A point in favour of the EKF+MPC configuration can be seen in Figure 12, which shows the control error. It is easy to see that the MPC controller allows for a lower control error than the other two configurations. As a matter of fact, this is one of the advantages of adopting an optimal control law. When looking at the remaining configurations,

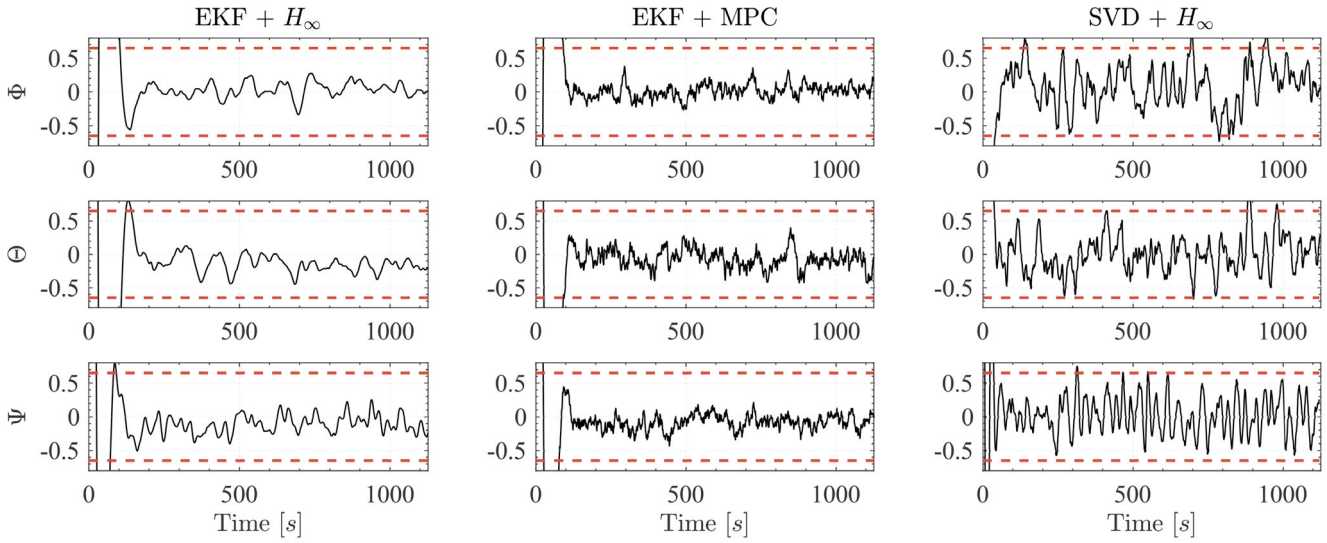

FIGURE 11 Absolute performance error (APE) on Euler angles for the three configurations, resulting from the nadir pointing simulation. The boundaries indicate the region in which the requirement defined in Table 1 is met.

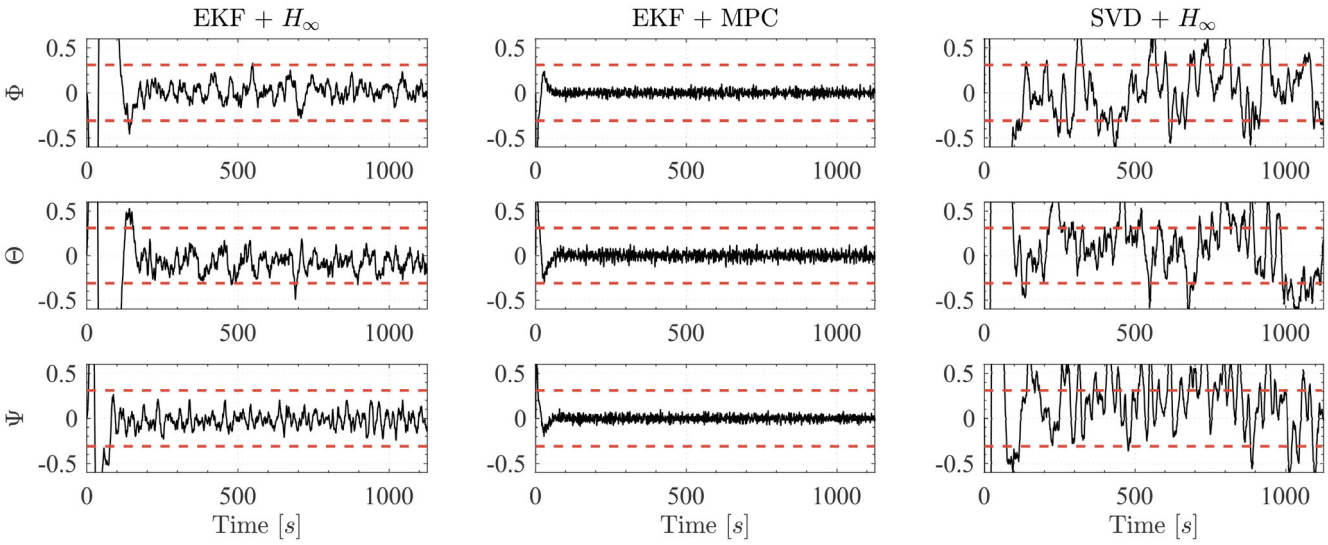

FIGURE 12 Control error (c) on Euler angles for the three configurations, resulting from the nadir pointing simulation. The boundaries indicate the region in which the requirement defined in Table 1 is met.

in the EKF+H_∞ case, the requirement is fulfilled to a large margin, whereas the SVD+H_∞ configuration fails to fit within the boundaries. The real advantage of combining the extended Kalman filter and H_∞ optimal output feedback controller can be seen in Figure 13. The figure shows the performance stability error (PSE), thus the difference between the instantaneous performance error at a given time t and the error value at an earlier time $t - \delta t$. It is immediately noticeable that the EKF+H_∞ configuration has a much smaller PSE than the other two and exhibits a trend with less noise, indicating that the properties of the H_∞ controller combined with those of the EKF result in good stabilization. In contrast, the EKF+MPC combination is the worst but at least meets the PSE requirement.

The results obtained clearly demonstrate that the proposed algorithmic combination exhibits superior performance compared to the other two configurations. This reaffirms the advantage of its utilization and underscores its efficacy.

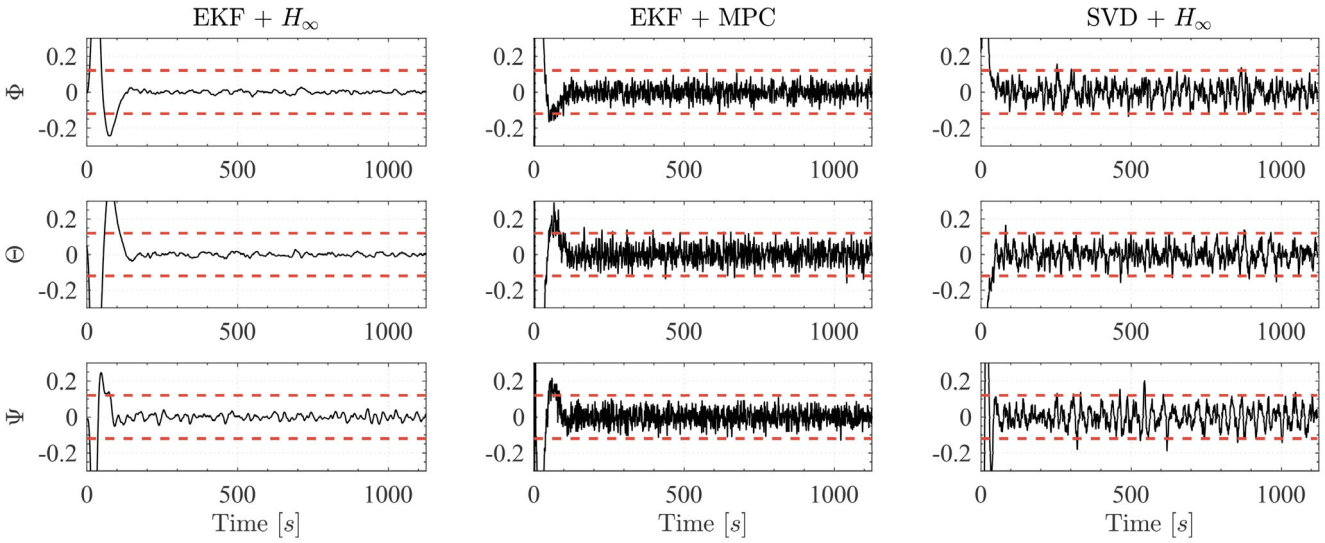

FIGURE 13 Performance stability error (PSE) on Euler angles for the three configurations, resulting from the nadir pointing simulation. The boundaries indicate the region in which the requirement defined in Table 1 is met.

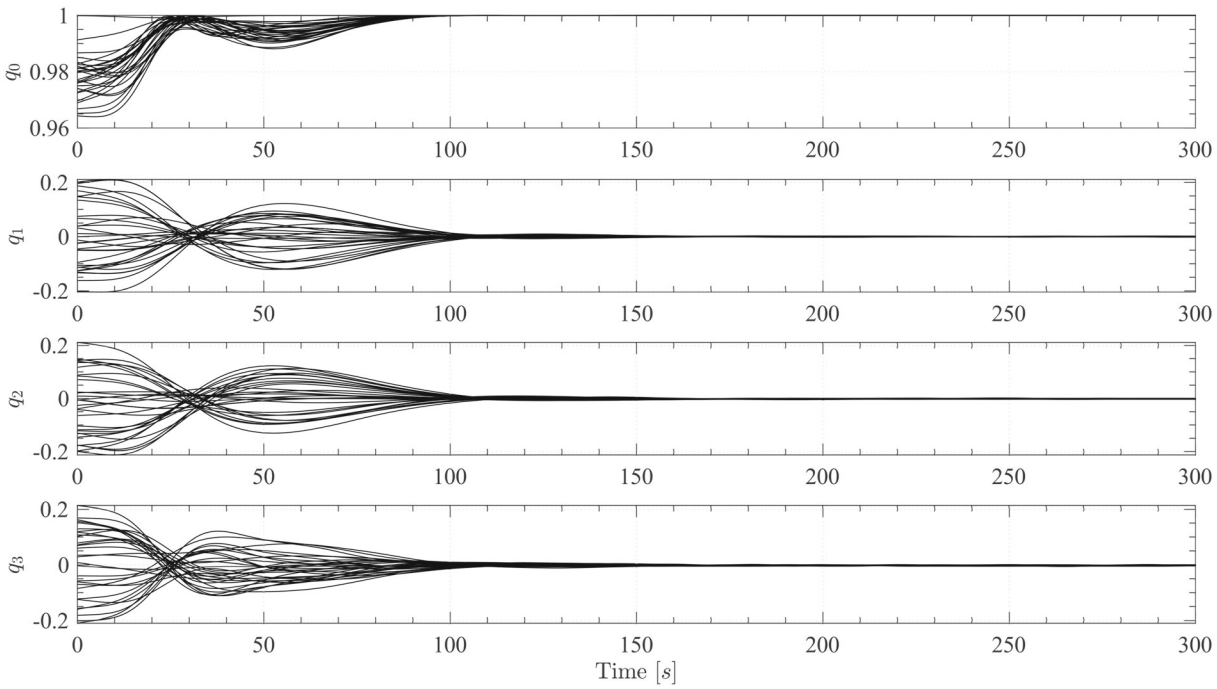

FIGURE 14 Quaternions resulting from the nadir pointing Monte Carlo simulation.

3.2.1 | Monte Carlo simulation

To test the robustness of the EKF+H_∞ configuration, a Monte Carlo simulation was carried out. The results of the 30 simulations are shown in Figures 14, 15, and 16. The simulations were carried out by setting the initial condition of the extended Kalman filter state vector equal to zero. This was also done to test the ability to converge to the desired state from an incorrect state estimate. Each simulation varies the initial conditions inside the range reported in Table 5.

From Figure 16, it can be seen that all requirements are met with a few exceptions.

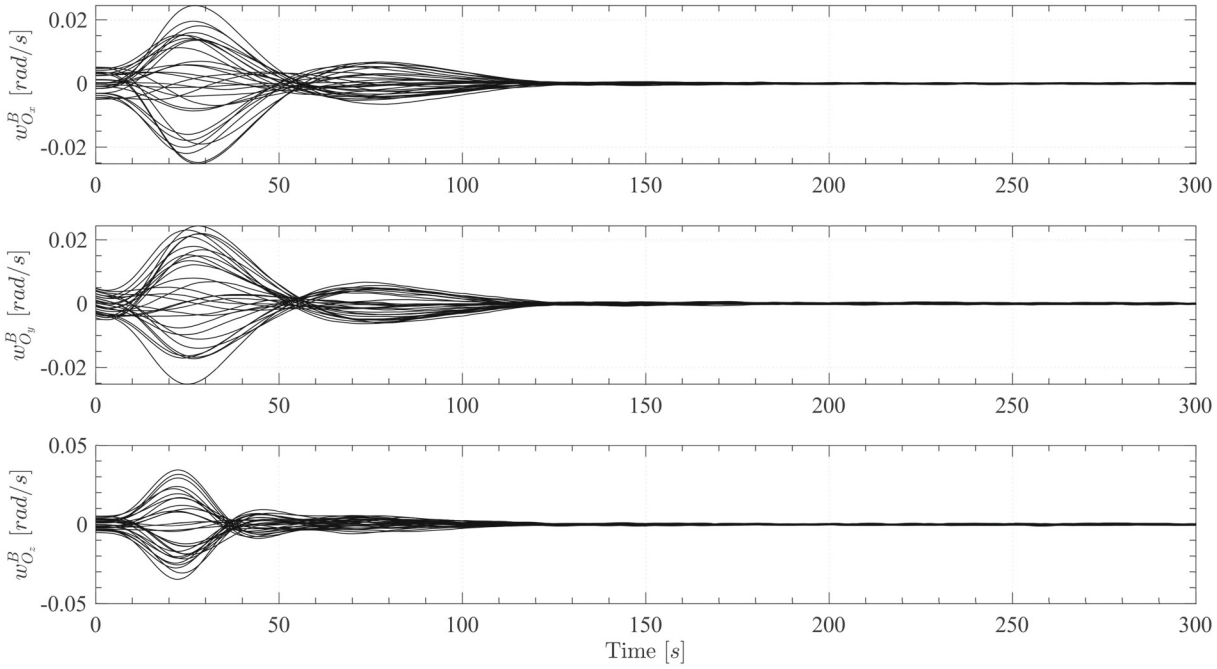

FIGURE 15 Angular velocities resulting from the nadir pointing Monte Carlo simulation.

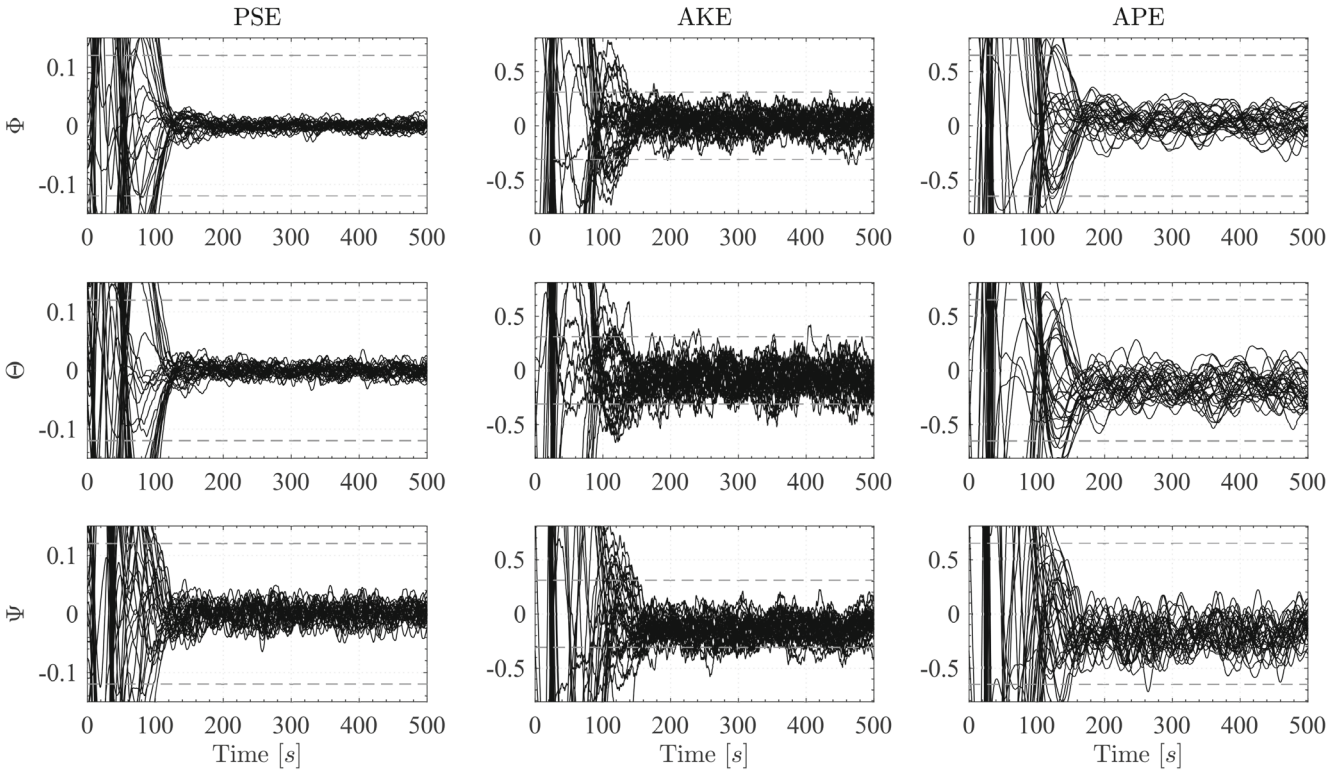

FIGURE 16 Extrinsic indicators resulting from the nadir Monte Carlo simulation.

TABLE 5 Initial conditions of the simulation with the boundaries of uncertainties.

Parameter	Value	Units	Uncertainties
Satellite Inertia $\begin{bmatrix} I_{xx} & I_{yy} & I_{zz} \end{bmatrix}$	$\begin{bmatrix} 0.0546 & 0.0546 & 0.0074 \end{bmatrix}$	$kg\,m^2$	±10%
Satellite mass (m)	4.548	kg	$\pm 1kg$
Initial attitude $\begin{bmatrix} \Phi & \Theta & \Psi \end{bmatrix}$	$\begin{bmatrix} 0 & 0 & 0 \end{bmatrix}$	deg	$\pm 25deg$
Initial angular velocity $\begin{bmatrix} \omega_x & \omega_y & \omega_z \end{bmatrix}$	$\begin{bmatrix} 0 & 0 & 0 \end{bmatrix}$	deg/s	$\pm 0.3deg/s$

4 | CONCLUSIONS

Performant attitude determination and control capabilities become fundamental for the actual and future CubeSat missions to enable a wide set of missions, in particular observation missions based on images taking. Stable and accurate pointing of the target requirements drive the ADCS design that should be achieved taking into account technology limitation. This study has illuminated a novel and promising avenue for enhancing control system performance in the context of satellite pointing stability. By intentionally applying the H-infinity optimal output feedback control technique, traditionally tailored for scenarios with partial state information, to a context with complete state knowledge, we have demonstrated the power of fusing established methodologies in an innovative manner. The integration of the Extended Kalman Filter's state estimation capabilities with the disturbance rejection and optimal control properties of the H-infinity controller has showcased remarkable advancements in pointing stability. Through comprehensive performance comparisons, we have substantiated the superiority of our approach over classical configurations. Other factors leading to the selection of this configuration are the greater control robustness due to the H_∞ controller and an easier implementation. The Model Predictive Control requires solving an optimization problem at each sampling time; instead, the H_∞ controller requires offline synthesis and can then be implemented discretely without requiring any special numerical arrangements. That results in a lower computational cost, which is very important in practice.

The proposed solutions were tested through numerous simulation sessions made on a dedicated simulation architecture that includes non linear dynamics and kinematics, and the effects of relevant disturbances torques caused by gravity gradient, air drag, solar radiation pressure, Earth's magnetic field and uncertainties elements.

ACKNOWLEDGMENTS

This work has been supported by Politecnico di Torino. The authors are very thankful to the anonymous reviewers for their precious indications that improved this paper.

CONFLICT OF INTEREST STATEMENT

The authors declare no potential conflict of interests.

DATA AVAILABILITY STATEMENT

The data that support the findings of this study are available from the corresponding author upon reasonable request.

ENDNOTE

*YALMIP is a toolbox for modeling and optimization in MATLAB.

ORCID

Manuel Pecorilla https://orcid.org/0009-0004-6291-3136

REFERENCES

1. Villela T, Costa CA, Brandão AM, Bueno FT, Leonardi R. Towards the thousandth CubeSat: a statistical overview. *Int J Aerosp Eng*. 2019;2019. doi:10.1155/2019/5063145
2. Kuiper H, Dolkens D. A cutting edge 6U CubeSat ADCS design for earth observation with sub-meter spatial resolution at 230–380 km altitude. *CEAS Space J*. 2020;12(4):613-621. doi:10.1007/s12567-020-00323-7
3. Schwartz N, Brzozowski W, Ali Z, et al. 6U CubeSat deployable telescope for optical earth observation and astronomical optical imaging. Paper presented at: 12180 of Space Telescopes and Instrumentation 2022: Optical, Infrared, and Millimeter Wave. SPIE. 2022:1073–1084. doi:10.1117/12.2627248

4. Millar P, Babu S. NASA earth science technology Demonstratinos on CubeSats. Paper presented at: IGARSS 2022-2022 IEEE International Geoscience and Remote Sensing Symposium. IEEE. 2022:7139–7140. doi:10.1109/IGARSS46834.2022.9883876
5. Speretta S, Turan E, Cervone A, et al. Lumio: a cubesat to monitor micro-meteroid impacts on the lunar farside. Paper presented at: 2022 IEEE Aerospace Conference (AERO). IEEE. 2022:1–8. doi:10.1109/AERO53065.2022.9843311
6. Corpino S, Stesina F, Calvi D, Guerra L. Trajectory analysis of a CubeSat mission for the inspection of an orbiting vehicle. *Adv Aircraft Spacecraft Sci*. 2020;7(3):271-290. doi:10.12989/aas.2020.7.3.271
7. Corpino S, Stesina F. Inspection of the cis-lunar station using multi-purpose autonomous Cubesats. *Acta Astronaut*. 2020;175:591-605. doi:10.1016/j.actaastro.2020.05.053
8. Tomio H, Thieu A, Gagnon A, et al. Commercially available imaging payloads for CubeSat earth observation missions. Paper presented at: 2022 IEEE Aerospace Conference (AERO). IEEE. 2022:1–19. doi:10.1109/AERO53065.2022.9843446
9. ESA-ESTEC. ECSS-E-ST-60-10C – Control Performance. 2008 https://ecss.nl/standard/ecss-e-st-60-10c-control-performance/. European Cooperation for Space Standardization
10. Yost B, Weston S, Benavides G, et al. State-of-the-Art Small Spacecraft Technology. 2021 https://ntrs.nasa.gov/api/citations/20210021263/downloads/2021SOAfinal508updated.pdf
11. Xia X, Sun G, Zhang K, et al. Nanosats/cubesats adcs survey. Paper presented at: 2017 29th Chinese Control and Decision Conference (CCDC). IEEE. 2017:5151–5158. doi:10.1109/CCDC.2017.7979410
12. Markley FL, Crassidis JL. *Fundamentals of Spacecraft Attitude Determination and Control*. Vol 1286. Springer; 2014.
13. Leomanni M, Garulli A, Giannitrapani A, Scortecci F. All-electric spacecraft precision pointing using model predictive control. *J Guid Control Dynam*. 2015;38(1):161-168. doi:10.2514/1.G000347
14. Mammarella M, Lee DY, Park H, Capello E, Dentis M, Guglieri G. Attitude control of a small spacecraft via tube-based model predictive control. *J Spacecraft Rockets*. 2019;56(6):1662-1679. doi:10.2514/1.A34394
15. Hegrenæs Ø, Gravdahl JT, Tøndel P. Spacecraft attitude control using explicit model predictive control. *Automatica*. 2005;41(12):2107-2114. doi:10.1016/j.automatica.2005.06.015
16. Zhang H, Zhao X, Wang H, Zong G, Xu N. Hierarchical sliding mode surface based adaptive actor critic optimal control for switched nonlinear systems with unknown perturbation. *IEEE Trans Neural Netw Learn Syst*. 2022. doi:10.1109/TNNLS.2022.3183991
17. Zhang H, Wang H, Niu B, Zhang L, Ahmad AM. Sliding mode surface based adaptive actor critic optimal control for switched nonlinear systems with average dwell time. *Inform Sci*. 2021;580:756-774. doi:10.1016/j.ins.2021.08.062
18. Tayebi A. Unit quaternion-based output feedback for the attitude tracking problem. *IEEE Trans Automat Contr*. 2008;53(6):1516-1520. doi:10.1109/TAC.2008.927789
19. Capua A, Shapiro A, Choukroun D. Spacecraft attitude control using nonlinear H-infinity output-feedback. Paper presented at: AIAA Guidance, Navigation, and Control (GNC) Conference. AIAA. 2013:4793. doi:10.2514/6.2013-4793
20. Alken P, Thébault E, Beggan CD, et al. International geomagnetic reference field: the thirteenth generation. *Earth Planets Space*. 2021;73(1):1-25. doi:10.1186/s40623-020-01288-x
21. Vallado DA. *Fundamentals of Astrodynamics and Applications*. Vol 12. Springer Science & Business Media; 2001.
22. Caverly RJ, Forbes JR. LMI Properties and Applications in Systems, Stability, and Control Theory. arXiv preprint arXiv:1903.08599. 2019. doi:10.48550/arXiv.1903.08599
23. De Oliveira MC, Geromel JC, Bernussou J. Extended H 2 and H norm characterizations and controller parametrizations for discrete-time systems. *Int J Control*. 2002;75(9):666-679. doi:10.1080/00207170210140212
24. Scherer C, Gahinet P, Chilali M. Multiobjective output-feedback control via LMI optimization. *IEEE Trans Automat Contr*. 1997;42(7):896-911. doi:10.1109/9.599969
25. Lofberg J. YALMIP: a toolbox for modeling and optimization in MATLAB. Paper presented at: 2004 IEEE International Conference on Robotics and Automation (IEEE Cat. No. 04CH37508). IEEE. 2004:284–289. doi:10.1109/CACSD.2004.1393890

How to cite this article: Pecorilla M, Stesina F. Novel extended Kalman filter + $\mathbf{H}_\infty$ optimal output feedback control configuration for small satellites with high pointing stability requirements. *Int J Robust Nonlinear Control*. 2024;34(5):2991-3010. doi: 10.1002/rnc.7119